Multi-fidelity Aerodynamic and Acoustic Design and Analysis of a Heavy-lift eVTOL

Tao Zhang [1], George N. Barakos [2]

CFD Laboratory, School of Engineering, University of Glasgow, Glasgow, U.K.

Furqan [3], Malcolm Foster [4]

GKN Aerospace, Bristol, U.K.

Abstract

This work presents the processes used to support the preliminary design of a large eVTOL vehicle at the University of Glasgow in collaboration with GKN Aerospace. To support the GKN heavy-lift eVTOL design, known as Skybus, a range of tools of various fidelity levels were adopted and integrated. The paper first proposes and demonstrates a multi-fidelity approach for the vehicle propeller design. The propeller pitch-RPM maps were also proposed and were demonstrated to be an efficient tool for the intuitive performance visualisation, fast and accurate performance prediction, and graphic interpolation of operating conditions. High-fidelity CFD simulations of the complete Skybus vehicle in forward flight with two and four operating propellers were later carried out. The propeller operating conditions were determined through the performance maps. Near-field acoustics of the vehicle was extracted directly from the flow solutions. Detailed discussions of the flow details and the acoustic sources due to aerodynamic interference were presented. Far-field noise features were also computed using the FW-H equations and the CFD solutions. The noise levels of the heavy-lift vehicle were about 70-75 dB perceived on the ground. Considerable differences in the noise directivities of two- and four-rotor configurations were observed and discussed.

1 Introduction

Following growing public demands for improved urban transportation, Urban Air Mobility (UAM) concepts have drawn considerable attention from industry and academia in recent years. Thanks to significant advancements in electric propulsion systems, many of the UAM vehicle designs adopted more unconventional configurations for improved performance and reduced carbon/noise emissions, which often feature multi-rotor systems, convertible designs, and electrical Vertical Taking-Off and Landing (eVTOL). Several conceptual designs or prototypes have been unveiled by manufacturers such as Rolls-Royce[1] and Airbus[2]. It is notable, however, that most existing eVTOL designs are aimed at the capacity of 2 to 6 passengers, as an air taxi or a personal vehicle. The possibility of heavy-lift eVTOL vehicles has been rarely explored.

In light of this, GKN Aerospace have proposed the Skybus concept as part of a techno-economic feasibility assessment under the UK ISCF Future Flight Challenge. Skybus aims to take the "Park and Ride" concept into the air, for mass transit over extremely congested routes thus eliminating the 2-dimensional

constraints of current surface transport modes including cars, trains, and buses. One application example looks at commuting routes around the London M25 circle into the centre of London within 15 minutes at the maximum capacity of 30 passengers. Compared to the small eVTOL designs, the large size of the Skybus makes it ideal to serve as future aerial public transport, but it poses extra challenges to the vehicle design in terms of the performance, dynamics, and especially the acoustics.

At this preliminary stage, the Skybus concept is designed to be a multi-rotor compound rotorcraft with six wing-tip-mounted, tiltable propellers and three sets of stub lifting surfaces. The initial vehicle sizing and airframe design was completed using simple lifting line and momentum theories. The propellers are envisaged to be powered by electrical motors, thereby having both pitch and RPM regulations. In hover, or vertical landing/taking-off, all propellers can be tilted vertically to provide thrust countering the vehicle weight and acceleration. Wing flaps can also be deployed to reduce the downwash blockage. In forward flight, lift is provided by the wings. The propellers are tilted horizontally to provide thrust countering the overall drag. In forward mode, each propeller is designed be either operating, or stopped and feathered, or folded. It can be easily noted that the forward flight configurations are not unique due to the redundancy brought by the large number of propellers. The forward flight drag may be easily countered by just one or two sets of the propellers, which are designed to lift the entire vehicle weight in hover. Therefore, this work also presents investigations and comparisons of configuration options in forward flight.

As the key component of a multi-rotor system, the propeller design and accurate performance analysis are of vital significance to the overall vehicle design. For the aerodynamic design and analysis of propellers or rotors, tools of various fidelity levels are commonly used. Low-fidelity tools or methods, e.g. Blade Element Momentum Theory or panel methods [3, 4], are capable of quick performance evaluation of a range of designs thanks to their low computational costs. However, the results are often associated with high uncertainty levels due to their limitations to handle complex flow physics such as compressibility, tip vortices, and flow separation. High-fidelity methods, typically modern CFD methods [5, 6, 7], on the other hand, are capable of providing accurate performance predictions and elaborate flow details for further acoustic or aeroelastic evaluations. However, the computational costs can be excessively high, hence their usage is often restricted to only narrow regions of the design space. A multi-fidelity design and analysis framework bridging the benefits of low- and high-fidelity would allow their disadvantages to be mutually compensated.

For the aerodynamic/acoustic analysis of the complete vehicle, the complexity of the Skybus configuration indicates strong aerodynamic interference and complicated aero-acoustic footprints. For the aerodynamic modelling and analysis of such vehicles, low-fidelity methods, such as lifting line or panel method, can provide rough performance estimations, but their results suffer from strong uncertainty due to their inherent incapability to resolve complex phenomena. For the subsequent aero-acoustic analysis, which requires accurate information from the aerodynamic solutions, the inaccuracy in the low-fidelity results is often con-

siderable. High-fidelity methods are hence desirable for the accurate numerical modelling of the aerodynamics, and especially the acoustics.

This work presents high-fidelity numerical investigations of the aerodynamics and acoustics of the GKN Skybus concept. The proposed multi-fidelity design framework combines fast low-fidelity parametric evaluations and high-fidelity gradient-based optimisation and performance analysis. Propeller pitch-RPM performance maps were then proposed and demonstrated to be efficient tools for the intuitive performance visualisation, fast and accurate performance prediction, and graphic interpolation of operating conditions. High-fidelity simulations of the complete Skybus vehicle in forward flight were then carried out and two different configurations were considered. Near-field acoustic results were directly extracted from the flow solutions, and far-field noise propagations were computed following acoustic analogy methods using the CFD solutions as the input. Detailed analyses and comparisons of the aerodynamics and acoustics of the two configurations are presented.

2 Numerical Methods and Tools

2.1 Multi-fidelity Propeller Analysis and Design Framework

The flowchart of the proposed multi-fidelity analysis and design framework are shown in Figure 1. The framework consists mainly of two stages, i.e. the low-fidelity and high-fidelity stages, and stages are bridged by an automatic CAD and mesh generation framework that converts the low-fidelity outputs into inputs to the high-fidelity stage. The framework aims to bridge the benefits of low- and high-fidelity methods, and allows for their disadvantages to be minimised.

In the low-fidelity stage, an enormous set of potential designs are quickly assessed using low-fidelity methods. The low-fidelity analyses were carried using the XRotor code [3]. The low-fidelity stage outputs an initial performance database, as well as, an initial optimal design, subject to constraints. This initial design corresponds to the global optimum within the investigated design space. However, it should be stressed that this optimal result is associated with high levels of uncertainty due to the low-fidelity nature. Nonetheless, it can serve as a fine input to the high-fidelity stage for further analysis and design optimisation.

The low-fidelity design output is then channelled into the high-fidelity stage through an automatic geometry and mesh composition framework of the HMB3 toolkit [8, 9]. High-fidelity CFD simulations are then carried out using the HMB3 solver to evaluate the performance of the low-fidelity design input. High-fidelity gradient-based shape optimisation is launched to further improve the propeller design subject to constraints. Typically, gradient-based optimisation offers only local optima close to the initial input. In this case, however, the final design output of the high-fidelity stage is highly likely to be, or at least very close to, the global optimum design solution subject to consistent objectives and constraints. This is because the initial input comes from a global scan of the design space from the low-fidelity stage. Although associated with high uncertainty, this input is already close enough to the global optima.

The low-fidelity results narrow the design space to be explored by high-fidelity methods, thereby reducing

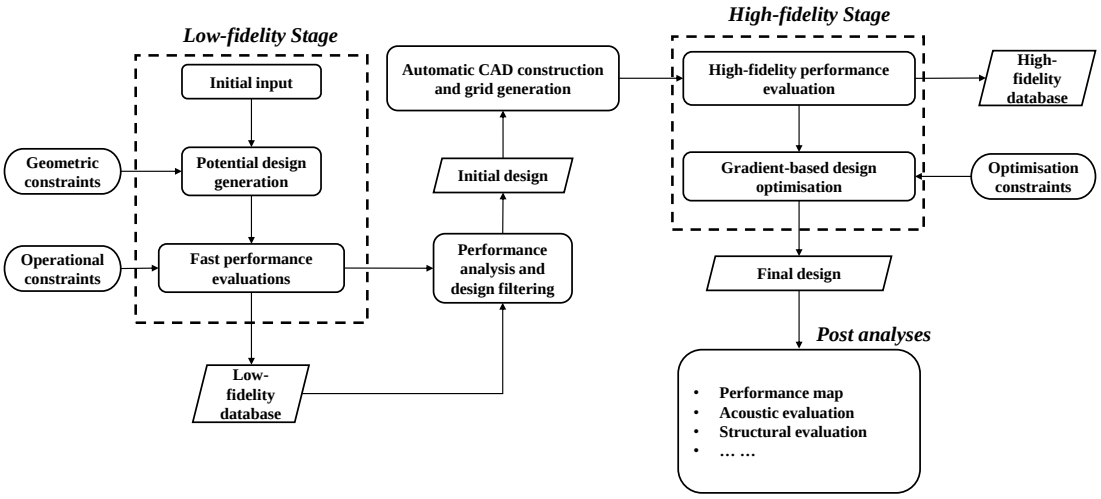

Figure 1: Flowchart of the proposed multi-fidelity analysis and design framework for propellers.

the computational cost. The high-fidelity analysis and optimisation then eliminates the uncertainty associated with the low-fidelity methods. High-performance propeller designs are hence delivered at much reduced computational costs without compromising the modelling accuracy. Compared to only adopting low-fidelity methods, the proposed framework has improved accuracy, and the computational cost is moderately increased. However, compared to using high-fidelity methods only, the framework has significantly reduced computational costs thanks to the narrower design space to be explored.

The proposed framework also features high-levels of automation and versatility. The framework handles the sampling, computation, data processing/conversion, and optimisation mostly automatically. Only minor user interventions and decision making are necessary. The analysis tools and methods, including the parametrisation and optimisation, can be easily replaced, if necessary. For instance, the gradient-based optimisation block at the high-fidelity stage in Figure 1 can be replaced by gradient-free algorithms, if necessary. In addition, databases of multiple fidelity levels are also provided by this framework. These results can be carefully integrated to provide more guidance for further design and analysis.

2.2 Helicopter Multi-Block 3 (HMB3) Toolkit

2.2.1 HMB3 Flow Solver

As a high-fidelity flow solver and the core of the high-fidelity analysis stage, the in-house Helicopter Multi-Block 3 (HMB3) [10, 11] CFD code was used in the present work. The code has been widely used in simulations of rotorcraft flows [12, 13, 14, 15]. HMB3 solves the Unsteady Reynolds Averaged Navier-Stokes (URANS) equations in integral form using the Arbitrary Lagrangian Eulerian (ALE) formulation for time-dependent domains, which may include moving boundaries. The Navier-Stokes equations are discretized using a cell-centered finite volume approach on a multi-

block, structured grid:

$$\frac{d}{dt}\left(\mathbf{W}_{i,j,k}V_{i,j,k}\right) = -\mathbf{R}_{i,j,k}\left(\mathbf{W}_{i,j,k}\right), \tag{1}$$

where i,j,k represent the cell index, $\mathbf{W}$ and $\mathbf{R}$ are the vector of conservative flow variables and residual respectively, and $V_{i,j,k}$ is the volume of the cell i,j,k. To evaluate the convective fluxes, Osher-approximate Riemman solver is used, while the viscous terms are discretized using a second order central difference scheme. The 3^{rd} order MUSCL (Monotone Upstream-centered Schemes for Conservation Laws) approach was used to provide high-order accuracy in space. The chimera/overset grid method [16] was extensively used in this work. In the present work, simulations were performed with the $k-\omega$ SST [17] turbulence model. The non-intertia Rotating Reference Frame (RRF) method[6] in HMB3 was also adopted for simulations with rotational periodicity, such as rotors in hover or axial flight.

The HMB3 solver is also equipped with an automatic grid generation framework [8, 9]. The automation framework is capable of delivering composed geometries and high-quality, ready-to-run structured grids for various purposes, upon simple definitions or existing CAD models, with minor human interventions. It greatly eases the efforts required for the preparation of high-quality grids for numerical analysis. This framework was used in the present work to bridge the low-fidelity and high-fidelity stages.

2.2.2 HMB3 Adjoint Solver and Gradient-based Optimisation

The adjoint method[18][11] is known for its efficient handling of large numbers of design variables with few objective functions. This is especially suitable for the current optimisation study of propeller blades, which involves many design variables governing blade shapes with just a few objective/constraint functions e.g. the overall thrust and torque.

In the context of CFD analysis, a typical objective function I can be explicitly defined as $I(\mathbf{W}(\alpha),\alpha)$, which is a function subject to the design variable vector α and the flow variables $\mathbf{W}(\alpha)$. The flow variables still satisfy the governing equation in the form $\mathbf{R}(\mathbf{W}(\alpha),\alpha)=\mathbf{0}$.

The core of many gradient-based optimisation problems, as also involved in this work, is to solve the sensitivity equation of I relative to the design variables α as follows:

$$\frac{dI}{d\alpha} = \frac{\partial I}{\partial \alpha} + \frac{\partial I}{\partial \mathbf{W}}\frac{\partial \mathbf{W}}{\partial \alpha}. \tag{2}$$

The difficulties solving this equations lie in the second term on the RHS, especially the term $\frac{\partial \mathbf{W}}{\partial \alpha}$. It can be implicitly derived from the governing flow equations, but the computational requirement would be excessive when using direct differentiation or finite differences because of the large amount of design variables.

Alternatively, introducing an adjoint vector λ correlating the cost function and the governing equations, the sensitivity equation 2 can be recast in the adjoint form as :

$$\left(\frac{\partial \mathbf{R}}{\partial \mathbf{W}}\right)^T\lambda = -\left(\frac{\partial I}{\partial \mathbf{W}}\right)^T. \tag{3}$$

$$\frac{dI}{d\alpha} = \frac{\partial I}{\partial \alpha} + \lambda^T\frac{\partial \mathbf{R}}{\partial \alpha}. \tag{4}$$

The major effort solving the sensitivity equation aligns with solving the adjoint vector λ coupled in the linear system in Equation 3. This linear system scales

with the number of objective functions and is irrelevant to the design variables. This property makes the adjoint formulation especially suitable for aerodynamic shape optimisation. Details of the HMB3 adjoint formulations can be found in previous optimisation studies of rotors, wings, and ducted propellers [11, 6, 7].

With the gradients computed, design changes can be determined to improve the objective performance subject to constraints. The Sequential Least-Square Quadratic Programming (SLSQP) algorithm[19] as provided in the *NLopt* library [20] is used as the optimiser in this study. The SLSQP algorithm approximates and solves the objective functions with a sequence of least-square/quadratic programming problems. The constraints are approximated with linear functions. This algorithm is frequently used due to its effectiveness and efficiency. Based on the initial objective, constraint, and gradient information, the optimiser solves for the searching directions in the design space and step sizes. The design variables are then modified accordingly, and new CFD computations are launched to acquire the new cost function value and gradients. The iterations continue until the gradients or step size are approaching zero, or the maximum iteration has been reached. An advanced mesh deformation algorithm is implemented in HMB3 based on Inverse Distance Weighting (IDW) interpolations[21, 6, 22] to bridge the shape deformation and the adjoint system. More details of the optimisation framework can be found in Refs[7, 23].

2.2.3 Near-field and Far-field Acoustic Computations

In the present study, the near-field acoustics was directly derived from pressure fields resolved by high-fidelity HMB3 simulations. The sound pressure signals were extracted by subtracting the time-averaged pressure field from raw unsteady data. This direct approach included all acoustic sources in the near-field, subject to the near-field CFD resolution. The similar approach has been used in acoustic analyses of propellers, ducted propellers, and eVTOL vehicles using HMB3 [24, 7, 1]. This approach requires high-order schemes and fine spatial/temporal resolution. For the current acoustic study, the 3rd-order MUSCL scheme was used.

For simulations of the Skybus vehicle in forward flight, the near-field background grid was carefully tuned to guarantee at least 10 mesh points for the wave length at 10 times the BPF(about 360 Hz), in the 20-metre proximity. Most near-field acoustic evaluations were carried out within 15-metre proximity of the vehicle. The simulations adopted a time step of $1^{\circ}/step$ of the propeller revolution. This temporal resolution corresponded to at least 60 sampling points for the dominant BPF noise. Smaller steps were desirable but were not used due to high computational costs.

In this work, the far-field acoustics was efficiently calculated using the FW-H equation [25], following the Farassat Formulation 1A [26], taking as input CFD solutions of the surface pressure fields. The formulation has been widely used for far-field noise predictions of aircraft, wind turbines [27], and propellers [7, 28, 29]. The current far-field acoustic computations were carried out using the in-house acoustic solver HFWH2 (Helicopter Ffows Williams-Hawkings 2), which has been used in previous acoustic computations of propellers and ducted propellers [7, 29]. Extensive code-to-code comparisons have also been performed in order

to verify the current implementation [28].

The Farassat Formulation 1A [26] solves surface terms of the FW-H equation, i.e. the thickness noise and the loading noise, in the time domain through the introduction of the retarded time concept. The formulation results in two linear equations respectively for the thickness and loading components. The current far-field acoustic approach focused on the non-porous formulation, and ignored the quadrupole source which requires expensive integrations over volumes. This approach is reasonable considering the subsonic nature of the current study, and is efficient and sufficiently accurate for purposes of initial engineering analyses.

2.3 XRotor Code

The XRotor code is an open-source tool developed by Drela et.al. [3, 4, 30]) for performance predicting and design of propellers. The code is based on extended classic blade-element/vortex theories, in combination with lifting line and panel methods. It is capable of quickly predicting, or matching propeller performance for specific geometries, as well as solving inverse design problems. Nonetheless, the code relies heavily on accurate blade sectional aerodynamic inputs. Due to inherent limitations of the methods, it is also incapable of handling complex flow phenomena e.g. stall, flow separation, and strong compressibility. The XRotor is used in this work for as the low-fidelity tool for quick evaluation of the aerodynamic performance of a large set of propeller designs, but the delivered results are to be corrected by high-fidelity methods, later in the analyses.

2.4 Kriging Response Surfaces

The Kriging surrogate model [31] is a spatial interpolation method based on Gaussian regression. The current work adopted the Kriging model for purposes of data interpolation/extrapolation and visualisation. The Kriging model predicts the value of an unobserved evaluation point using a predictor function plus a small, stochastic variance as follows

$$Z(\mathbf{x}) = Z_0 + \epsilon(\mathbf{x}), \tag{5}$$

where $Z(\mathbf{x})$ is the prediction at the unknown location $\mathbf{x}$, and Z_0 is the mean value of the data set. $\epsilon(\mathbf{x})$ is a random variable depending on the distance between the unknown point and the sampling points and has the mean value of zero. The term $\epsilon(\mathbf{x})$ is determined based on prescribed correlation kernels and an existing sampling database. The current work adopts the Ordinary Kriging with Z_0 denoted by a constant and $\epsilon(\mathbf{x})$ assuming a normal distribution.

Compared to methods like radial-base functions or polynomial approximations, the benefits of the Kriging approximation are that it rarely encounters the issue of over-fitting. Additionally, it also provides uncertainty estimations of the predictions due to its stochastic nature. The drawbacks are the slightly larger computational costs for solving linear systems (which scales with the number of sampling points) and a few assumptions on the data set in terms of stationarity and compliance with normal distributions. In the present work, the Surrogate Modelling Toolbox (SMT) was adopted [32].

3 Multi-fidelity Propeller Design

3.1 Parametrisation and Sampling

For the low-fidelity stage in this study, only blade pitch and chord distributions were considered. This was mostly because the XRotor code was not able to handle more complex parametres such as blade sectional shapes, swept, anhedral/dihedral angles. The chord and pitch distributions along the blade radius were approximated using Bernstein polynomials, and the polynomial coefficients were used as the design variables.

Details of the initial input geometries to initiate the low-fidelity stage are presented in Table 1. These correspond to simple rectangular blades with a linear twist. It should be noted that the blade number was also included in the design and analysis process. Note that the solidity values of propellers with different blade counts were maintained the same to keep similar blade loadings. These initial geometric parametres were analysed using the simple Blade Element Momentum Theory subject to the given size and operation restrictions.

Table 1: Initial geometry inputs estimated using the BEMT.

Planform	rectangular	
Linear twist	-40	deg
Solidity	0.078	
Radius	3.25	m
Blade number	4, 5, 6	

The initial geometric inputs were approximated by Bernstein polynomials as shown in Figures 2(a) to 2(c). Two families of polynomials were used to represent the chord and local pitch distributions, respectively. Upon these simple initial inputs, the Latin Hypercube Sampling approach was used to generate a large set of potential designs to be evaluated. In Figure 2(a) to 2(c), each of the grey transparent lines represents a new pitch or chord distribution starting from the initial input. These were generated through orthogonal sampling within the design variable ranges. Note that the chord length near the blade root was restricted to avoid root overlapping for high blade numbers. The combinations of these new pitch and chord distributions comprise the large set of potential propeller designs. In this study, a total of 3000 designs were evaluated.

3.2 Low-fidelity Performance Evaluation and Filtering

The aerodynamic performance of these potential designs were quickly evaluated using the lower-order code XRotor [3] in an automated manner with the help of bash scripts. All designs assumed the same RPM as per the operational constraints. The evaluated performance results of the 4-, 5-, and 6-bladed designs are plotted in Figures 3(a), 3(b), and 3(c), respectively. Also plotted are the Figure of Merit (FoM) intervals to indicate the aerodynamic efficiencies of designs. It can be observed that, for each family of designs with a different blade number, the distribution of points forms a performance front. As the blade number was increased, the efficiency front of the propeller design was also increased.

The next step was to filter out the propeller designs that resides on the performance front and delivers the target thrust. This was achieved by trimming all potential designs to the target thrust through collective pitch angle changes, then ranking the designs according to their power requirements. This is illustrated in Figures 4(a) to 4(c) for the three families of designs. The

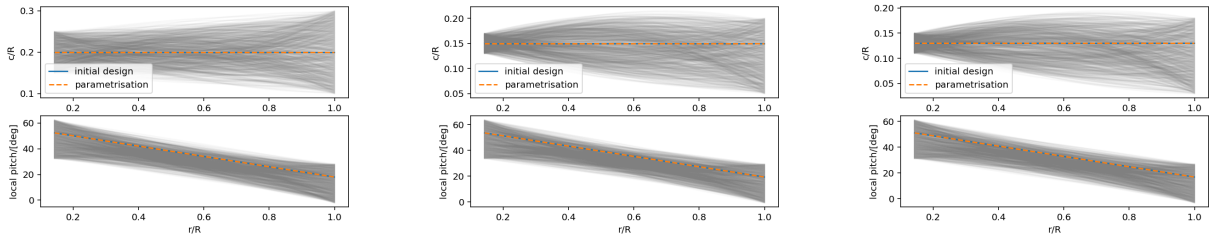

(a) Four-bladed designs. (b) Five-bladed designs. (c) Six-bladed designs.

Figure 2: Propeller shape parametrisation and sampling with different blade numbers. Each family of designs have 1000 sampling points.

vertical lines represent the thrust target. As can be noted, although all potential designs could be trimmed to provide the target thrust, including the simple initial inputs, some required significantly higher power input than others. The red crosses denote the best designs among the potential designs.

Figures 5(a) to 5(c) present comparisons between the initial designs and selected best designs, in terms of chord and twist distributions. Compared to the simple initial designs, the improved designs showed increased chord around the blade middle span, and reduced chord near the blade tip. Local pitch angles were reduced by about 10° near the blade root and were very slightly increased near the blade tip for all improved designs. Overall, these changes in the blade shapes were expected to shift more aerodynamic loading towards the middle span of the blades.

Table 2 presents more quantitative power comparisons between the initial and best designs while meeting the target thrust requested. It can be noted that the propeller performance improved following the increasing blade numbers for both initial and best designs. The maximum power reduction was about 6.6 % relative to the initial input for the five-bladed design. Still, among the improved designs, the six-bladed design showed the best performance with a 3% power reduction relative to the initial input.

Nonetheless, it should be stressed that these were results from low-fidelity design and analysis tools with higher levels of uncertainty. This is also why optimisation algorithms were not invoked in this stage, as the optimisation may suffer heavily from the uncertainty levels. High-fidelity numerical analyses and optimisation are presented in the next subsection to verify the performance predictions and to further improve the propeller design.

3.3 High-fidelity Analysis and Optimisation

The selected optimal designs of Figures 5(a) to 5(c) from the low-fidelity stage contained the blade shape definitions, but these needed to be converted into 3D shape in CAD systems and high-quality grids were also necessary for high-fidelity CFD analyses. This was achieved through an automatic mesh generation framework [8, 9] of the HMB3 toolkit. Using the blade shape definitions as the input parametres, geometries and fully-structured grids were automatically generated through this framework with minor human interventions.

The constructed propeller shapes are shown in Fig-

Table 2: Performance comparisons between the initial inputs and the low-fidelity optimised designs.

Blade number	Power input/[kW]		Power reduction / [%]
	Initial input	Low-fidelity optimised	
4	1215.26	1152.35	5.2%
5	1207.51	1127.481	6.6%
6	1145.09	1110.901	3.0%

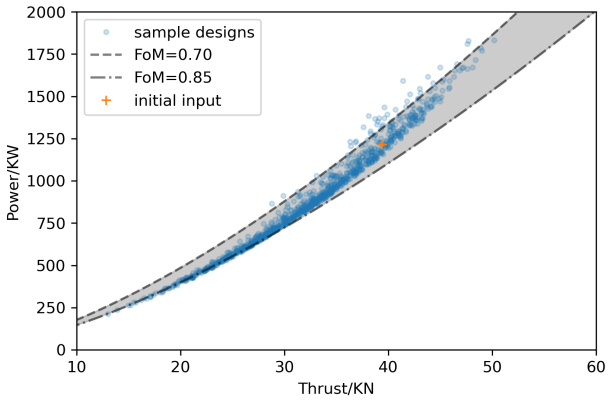

(a) Four-bladed designs.

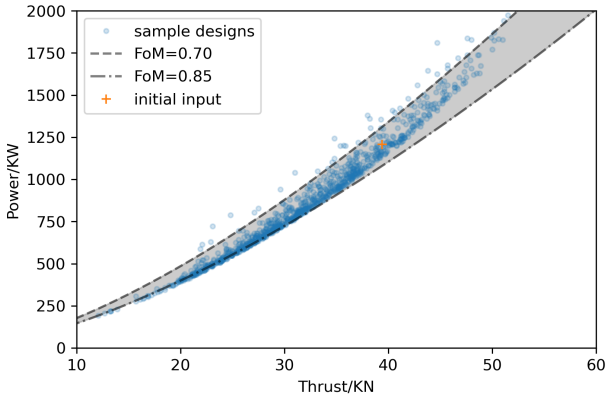

(b) Five-bladed designs.

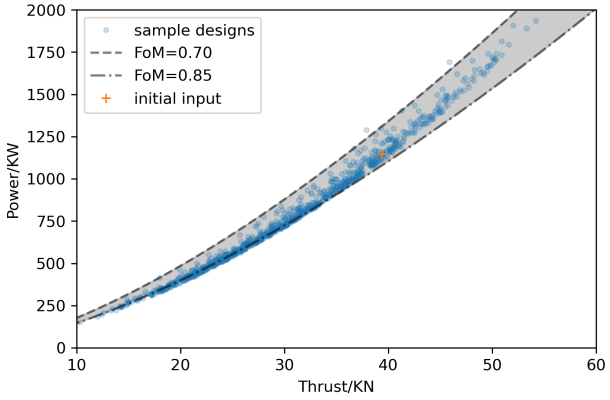

(c) Six-bladed designs.

Figure 3: Low-fidelity performance evaluations of potential designs.

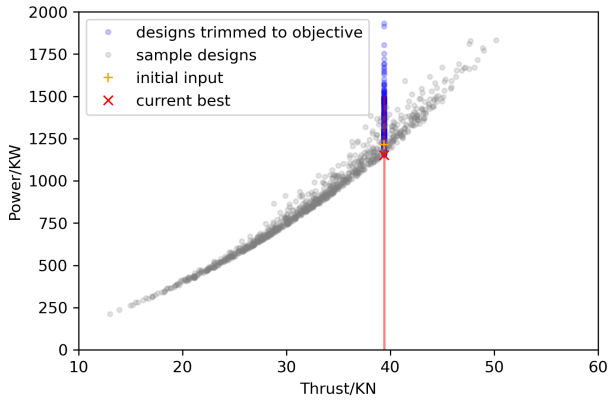

(a) Four-bladed designs.

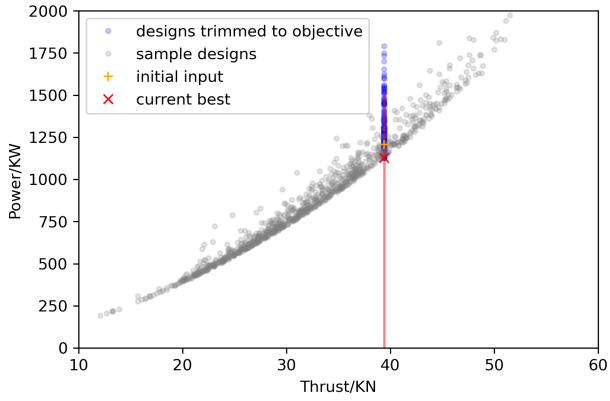

(b) Five-bladed designs.

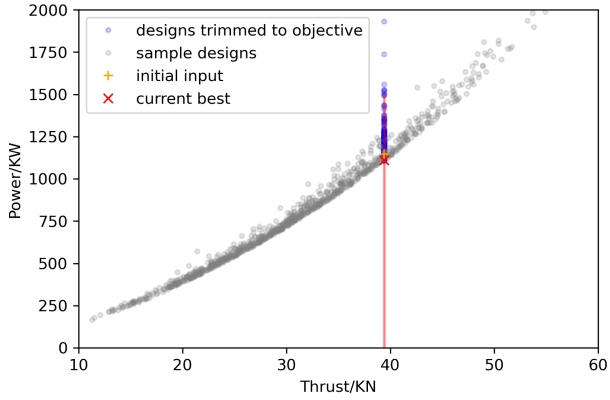

(c) Six-bladed designs.

Figure 4: Selecting the optimum design with the lowest power input in the low-fidelity stage.

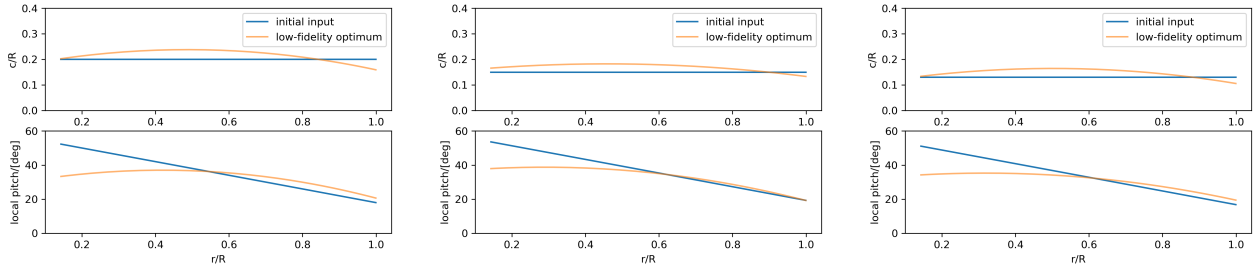

(a) Four-bladed designs. (b) Five-bladed designs. (c) Six-bladed designs.

Figure 5: Comparisons between the initial rectangular inputs and the selected low-fidelity optimum designs among the potential designs.

ures 6(a) to 6(c). The blade sections adopted the same NACA6412 airfoil shape, for simplicity. Fully-structured, body-fitted grids were generated enclosing the blade shapes. The high-fidelity HMB3 simulations were performed in the non-inertial rotating reference frame with the help of periodic and chimera boundaries. For simulations containing only one blade, about 6.3 million cells were used, which was more than sufficient according to previous simulations of propellers in axial flight [7]. The k-ω SST model was adopted for the simulations. The grids were carefully refined to ensure y+ around 1 near wall boundaries.

Flow solutions and wake structures of the initial designs at similar thrust levels are shown in Figures 7(a) to 7(c). The propeller wake structures were clean near the tips for all designs, but the flow solutions became complex near the blade roots. This was due to the low rotational speed, high pitch, high chord, and low sectional thickness at the root. As the blade number was increased, the root solutions improved. It is also interesting to observe that the helical tip vortex stayed closer to the blade as the blade number increased. This was caused by the slower downwash. It also indicates that a propeller design with too many blades would be prone to blade-vortex-interaction (BVI) at low thrust conditions.

Figures 8(a) and 8(b) present the high-fidelity performance evaluation of the propeller designs using HMB3, along with comparisons against XRotor results. The solid lines represent HMB3 results, while the dashed lines represent XRotor results. It is expected that the XRotor results deviate from the HMB3 predictions given their lower-order nature. The XRotor code slightly over-predicted the thrust and torque values for all the propeller designs. However, both methods predicted similar performance trends with RPM changes, and the differences between the methods were mainly offsets. It was also confirmed by the high-fidelity methods that the six-bladed propeller design was the best performance compared to the rest of the tested designs. Later performance analyses and design optimisation hence focused on the six-bladed design.

After high-fidelity performance evaluation of the design output from the low-fidelity stage, the next step is to further improve the design through high-fidelity methods. In the current work, gradient-based shape optimisation methods were adopted with the help of adjoint formulations. The low-fidelity design output was used as the initial design input to the optimisation loop.

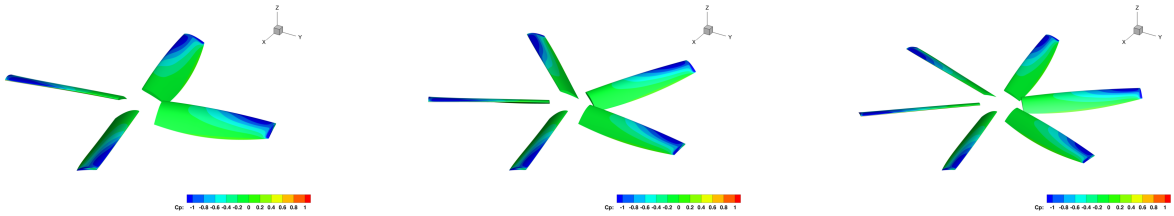

(a) Four-bladed designs. (b) Five-bladed designs. (c) Six-bladed designs.

Figure 6: Blade shapes constructed for HMB3 simulations from low-fidelity outputs.

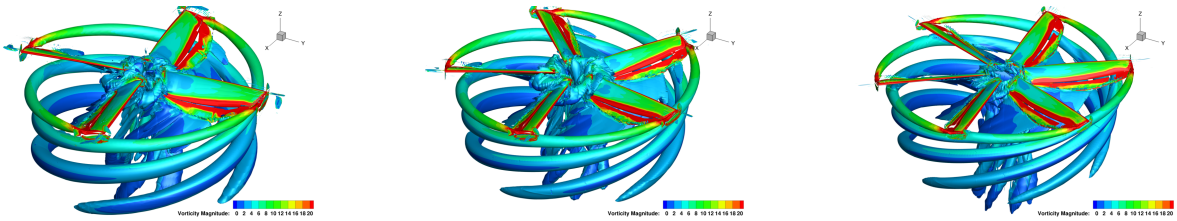

(a) Four-bladed designs. (b) Five-bladed designs. (c) Six-bladed designs.

Figure 7: Flow solutions and wake structures of the propeller designs, illustrated using q-criterion iso-surfaces coloured by vorticity magnitudes.

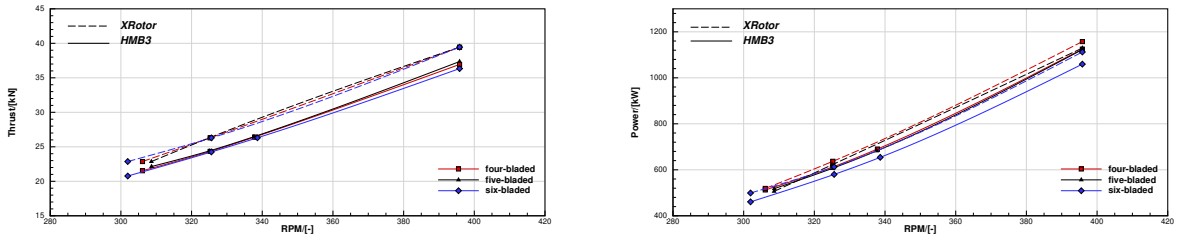

(a) Thrust. (b) Power.

Figure 8: Comparisons between low-fidelity and high-fidelity aerodynamic performance evaluations of the propeller designs.

As stated earlier, the optimisation study focused on the six-bladed design. The objective was to reduce the propeller torque, i.e. the power consumption, while maintaining the thrust. The design variables considered were again the blade pitch and chord distributions along the blade span. The sectional shapes were not included mainly due to restrictions of computational costs for the current study. This was a classic nonlinear optimisation problem subject to equality constraints. The optimisation problem was hence formulated as follows:

$$\begin{aligned} \text{Find: } & min(Q(\alpha_i, c_i)) \\ \text{by varying: } & (\alpha_i, c_i) \\ \text{subject to: } & |T(\alpha_i, c_i) - T_0| \leq \epsilon \end{aligned}$$

where $Q(\alpha_i, c_i)$ and $T(\alpha_i, c_i)$ are the propeller torque and thrust, respectively. (α_i, c_i) are Bernstein polynomial coefficients representing, respectively, the twist and chord distributions. T_0 is a reference thrust level that should be maintained, i.e. the target thrust.

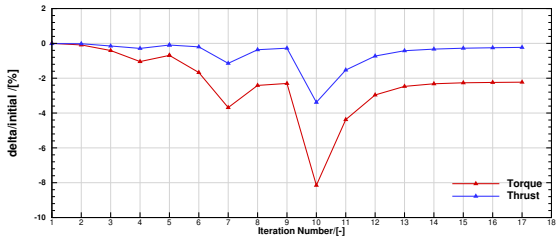

Figure 9: High-fidelity blade shape optimisation convergence history.

The optimisation was performed using a medium grid of about 4 million cells for a single blade, but the optimisation results were later verified using refined grids, and differences in the performance predictions were minor. The optimisation convergence history is shown in Figure 9. The optimisation converged within 17 iterations. The final results represent about 2.2% decrease in the torque and negligible changes in the thrust (about 0.2% decrease). The torque reduction corresponded to about 15 kW power reduction for the propeller, while changes in the thrust were only about 50 N.

Comparisons between the optimised and initial shapes are shown in Figures 10(a), 10(b), and 10(c). The optimisation increased the root pitch angle by about 2 degrees, and reduced the tip pitch angle by about 5 degrees, resulting in a highly increased twist across the blade span. The pitch angle at the 70% span was left unchanged. The 75% span pitch angle was reduced to 23.8°. The blade chord was increased from the root up until $r/R = 0.9$. Towards the tip, the blade chord was reduced. These changes shifted the loading from the blade tip towards the mid-span and root sections, leading to more evenly distributed blade loadings and approach the ideal loading distribution. Further performance evaluations at various operating conditions of the optimised propeller design are presented in later sections.

4 Propeller Pitch-RPM Performance Maps

For conventional pitch-regulated propellers, the performance output (either thrust, torque, or acoustic/elastic responses) under a fixed flight condition, can be written as a function $f(\beta)$ subject to the collective pitch setting β. Future eVTOL vehicles, however, are envisaged to have both pitch and RPM regulation for their propellers thanks to the adoption of electrical motors. The introduction of variable RPM control expands the function to $f(\beta, RPM)$. This certainly unlocks a much larger performance space and adds further operation flexibility, yet the problem dimensionality has also been increased due to the additional independent variable. This poses challenges for the propeller performance evaluation, as well as, the determination of operating conditions. This section hence used pitch-RPM performance maps that explicitly correlate and visualise various performance changes with changes in pitch/RPM settings.

Figures 11(a) to 11(d) present performance maps of the optimised propeller design output of the high-fidelity stage, in terms of thrust, power, efficiency (Figure of Merit), and Sound Pressure Levels (SPL) (measured at 10 m away, 2m below the propeller centre of rotation). In these figures, the horizontal axes represent blade pitch changes, while the vertical axes are the propeller RPM values. The contour maps represent the specific performance data within the pitch/RPM intervals. These maps present clear illustrations of various performance variations subject to pitch/RPM changes.

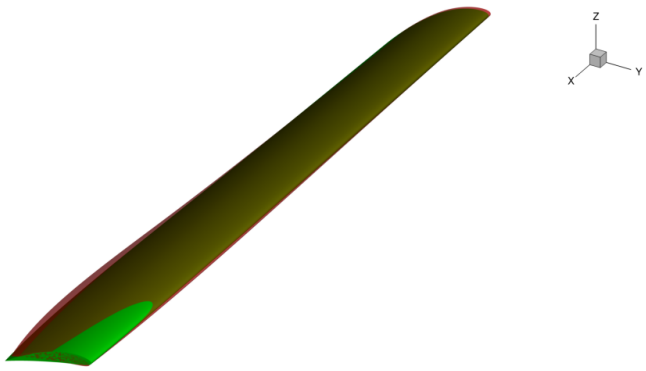

(a) Comparisons between the high-fidelity optimised and the low-fidelity optimum blade shapes. The green shape is the initial low-fidelity design, while the red is the high-fidelity optimised design.

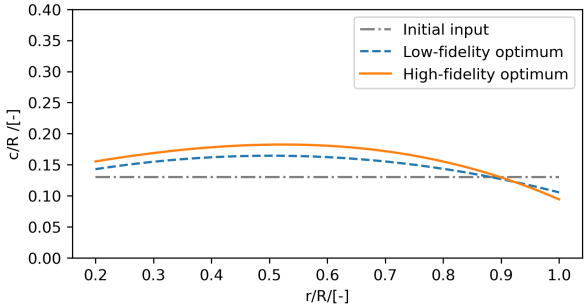

(b) Chord distribution changes.

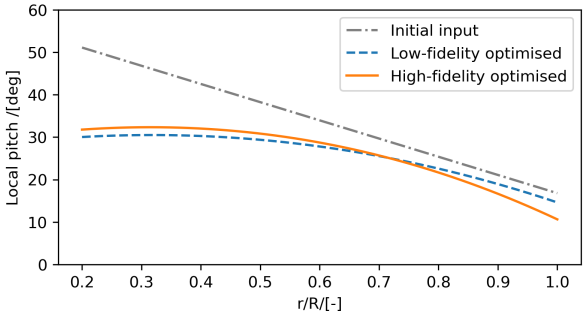

(c) Twist distribution changes.

Figure 10: Changes in the blade twist and chord distributions brought by the high-fidelity optimisation.

For instance, it can be easily observed from Figure 11(c) that the propeller has higher efficiency at lower pitch angles. From Figure 11(d), it can be noted that lower noise can be expected at lower pitch and RPM combinations.

In the present work, the propeller aerodynamic and acoustic performance at a specific pitch/RPM combination can be easily interpolated from the performance maps. More performance outputs, e.g. blade loadings or aero-elastic responses, can also be extracted and added to the performance maps to provide more comprehensive performance evaluation.

Potential operating conditions fulfilling specific thrust or power targets can also be determined using these maps. The dashed line in Figures 11(a) corresponds to the target thrust, and every pitch/RPM combination on this line would fulfil the thrust requirement. When overlapping this target thrust line with the other performance maps, as shown in Figures 11(b) to 11(d), the potential power, efficiency, and acoustic outputs subject to the thrust constraint are highlighted. It then becomes an intuitive graphic-based optimisation problem to choose the best operating condition subject to the equality thrust constraint. For instance, if one wishes to have maximum efficiency, the propeller collective pitch angle should be reduced while the RPM should be maintained around 380 according to Figure 11(c). On the contrary, if acoustic reduction is of the primary concern, the propeller pitch angle should be increased while the RPM should be reduced in this case according to the acoustic performance map in Figure 11(d). Depending on the specific objectives, the

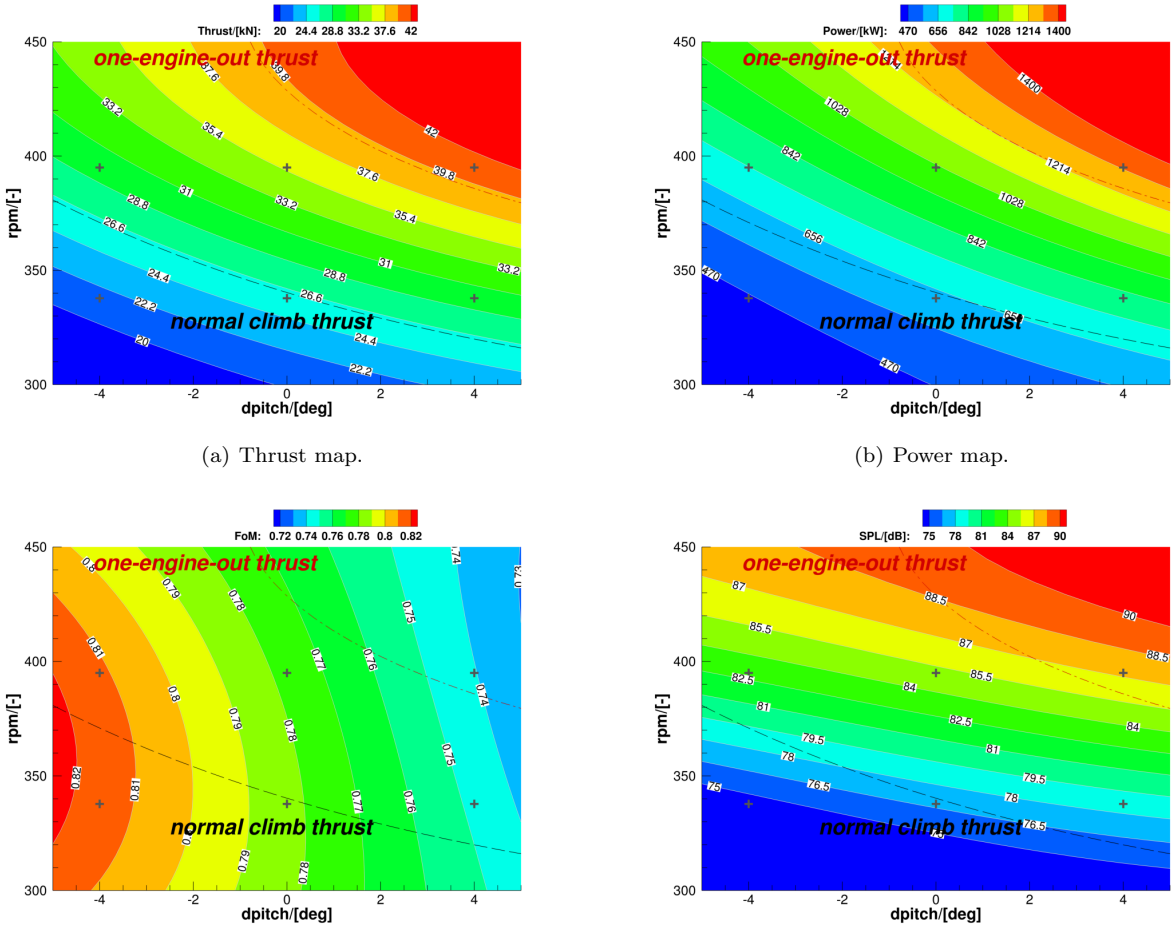

(a) Thrust map.

(b) Power map.

(c) Efficiency map.

(d) SPL at 10 meters away.

Figure 11: Aerodynamic and acoustic responses of the optimised propeller design in climb (baseline 75% blade span pitch angle 23.8°).

propeller operating condition can be easily determined through these performance maps.

These performance maps are essentially Kriging response surfaces constructed from high-fidelity performance results at sampling points, which are denoted by the "+" signs in Figures 11(a) to 11(d). In the current work, 6 sampling points were used within this narrow pitch/RPM interval. The accuracy of the Kriging approximation is validated using an extra sampling point as shown in Table 3. The differences between the Kriging predictions and the high-fidelity HMB3 predictions were within 1.5%. The computational cost of the HMB3 prediction, however, was significantly higher than the light-weight Kriging approximation. It should also be highlighted that, apart from the figures, the Kriging response surface can also be expressed as explicit functions to incorporate into analysis and optimisation loops.

5 Aerodynamic/Acoustic Evaluations of Skybus in Forward Flight

As mentioned earlier, the Skybus vehicle is a six-rotor, heavy-lift eVTOL design. Due to the large number of

Table 3: Differences between Kriging and HMB3 predictions of the propeller performance an extra, random sampling point. $P_{Kriging}$ denotes the Kriging predictions, and P_{HMB3} represents the HMB3 predictions.

	Thrust	Power	FoM	SPL
$P_{Kriging}/P_{HMB3} \times 100\%$	100.2%	101.2%	98.7%	101.3%

propellers, plenty of control and operating redundancy can be expected. The current design allows each of the six rotors to be either folded, stopped and feathered, or producing thrust at a certain pitch/RPM setting. As shown in Figure 12, several configurations are available for forward flight.

The simplest and cleanest configuration, in terms of aerodynamic interference, is the two-rotor configuration with four propellers folded (hence excluded from the modelling). While the six-rotor configuration, i.e. all propellers are rotating and producing thrust, would be most complex configuration with the highest aerodynamic interference. Assuming the same phase and rotation directions for all rotors, any performance output of the Skybus vehicle in forward flight, either aerodynamics or acoustics, would be a function dependent on the combinations of the pitch/RPM settings of each propellers. This function is expected to be highly nonlinear and complex, and certain pitch/RPM settings would surely deliver the optimum aerodynamic or acoustic performance. To explore the aerodynamic/acoustic performance output of the vehicle in forward flight, high-fidelity numerical methods are necessary considering the complex aerodynamic interference between rotors, lifting surfaces, and the airframe, yet the computational cost of assessing the complete function space through high-fidelity methods would be prohibitively high. This section presents high-fidelity HMB3 simulations of the simplest two-rotor configuration with all other rotors folded, as well as, a four-rotor configurations with the aft propellers stopped and feathered.

5.1 HMB3 Simulations of the Two-rotor and Four-rotor Configurations

The two-rotor configuration in forward flight refers to the configuration where only the two middle-wing propellers are operating, and all other rotors are assumed folded and therefore excluded from modelling, as shown in Figure 13(a). The four-rotor configuration in this work, as shown in Figure 13(b), refers to the configuration where the front and middle propellers are operating, while the aft propellers are stopped and feathered.

High-fidelity HMB3 simulations of the Skybus vehicle were carried out with the help of overset grids. The grid topology for the four-rotor configuration is presented in Figure 14. Grids for different components were generated separately with the help of the employed automatic grid generation, and assembled later using chimera methods for the CFD computation. The simulations adopted the URANS formulation with the k-ω SST turbulence model. The third-order MUSCL scheme was used to improve the spatial resolution. The first layer height of the grids near wall surfaces was carefully adjusted to keep the y+ value at 1. A symmetry plane was used as shown in Figure 14 to halve the computational domain and reduce the computational cost. In total, about 81 million cells were used for the half-model of the four-rotor configuration. For simulations of the two-rotor configuration, similar grid topology and simulation strategy was used, but the

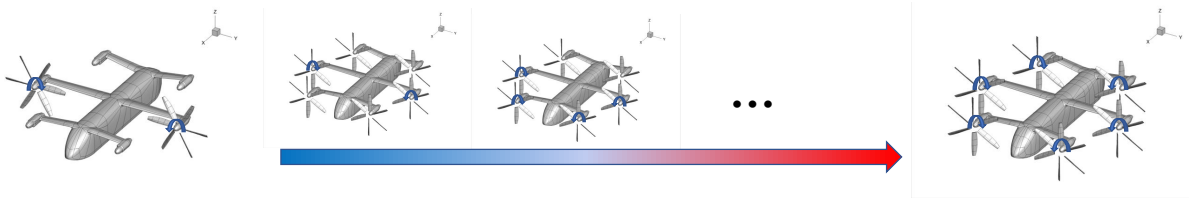

Figure 12: Configuration options for the Skybus in forward flight.

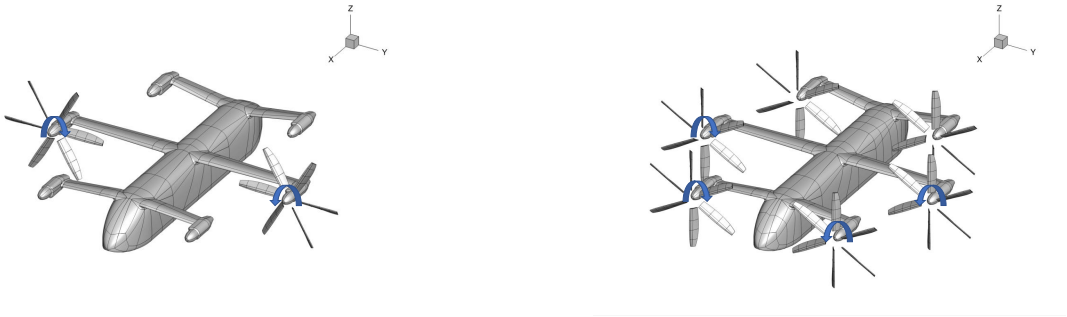

(a) Two-rotor configuration.

(b) Four-rotor configuration.

Figure 13: The two-rotor and four-rotor configuration of the Skybus vehicle for operations in forward flight.

overall cell number was reduced to about 47 million thanks to the removal of the front/aft propeller blades and their associated local refinement grids.

Both configurations were assumed to have the same forward flight speed of 90 m/s. The trimming condition was to have zero net drag while the overall lift can carry the vehicle weight. The operating conditions for the propellers, i.e. the pitch/RPM settings, were estimated from the drag of the isolated airframe and performance maps of the isolated propeller. This was achieved by interpolating for the pitch/RPM combination that can counter the airframe drag and requires the least amount of power input. Of course, such estimations did not take into account any installation effects or aerodynamic interactions. Nonetheless, these initial estimations were close to the actual solutions and accurate enough to initiate the high-fidelity simulations, and small corrections can be made upon the initial results.

The propeller operating conditions are presented in Table 4. In the current study, the propeller operating condition of the two-rotor configuration was directly estimated from the isolated performance, and trimmed forward flight was achieved without further corrections. For the four-rotor configuration, due to the strong interactions between the front and middle propellers, the pitch angles of the propellers were later adjusted by 1 to 2 degrees to achieve trimmed state.

5.2 Aerodynamic Performance Comparisons

Flow features of the two-rotor and four-rotor configurations resolved by the HMB3 simulations are presented in Figures 15(a) and 15(b). For the two-rotor configuration in Figure 15(a), the flow-filed was dominated by the clearly-resolved wakes of the two propellers, as well as, their interactions with downstream wings and nacelles. For the four-rotor configuration in Figure 15(b),

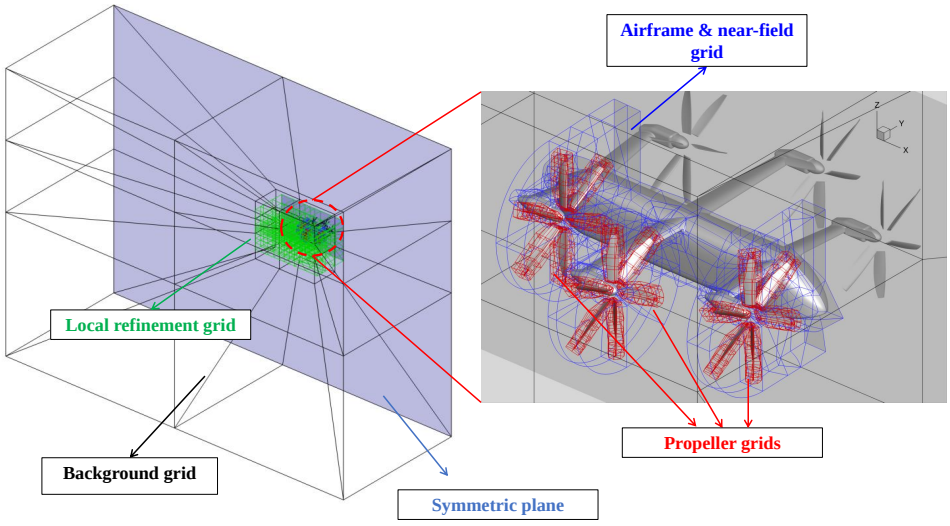

Figure 14: Grid details and overset topology for simulations of the Skybus in forward flight.

Table 4: Propeller operating conditions of the two- and four-rotor configurations. The 2-element tuples (β, RPM) represent the propeller pitch/RPM combinations.

Configuration	Front propeller	Middle propeller	Aft propeller
two-rotor	- (folded)	$(45.3°, 356)$	- (folded)
four-rotor	$(45.8°, 340)$	$(46.8°, 340)$	$(90°, 0)$ (feathered)

however, the flow features were much more complex. The wakes of the front propellers impinged partially on the middle propellers. The wakes of the front and middle propellers then joined together to attack the downstream wings the aft propellers. The stopped and feathered aft propellers managed to slightly reduce the complex, swirling flow. Still, strong and complex wakes were tailed behind the vehicle.

Table 5 presents comparisons of the propeller and vehicle performance between the two-rotor and four-rotor configurations. Note that all performance data was normalised by the propeller performance of the two-rotor configuration (T_0, Q_0) to reflect relative differences, where T_0 stands for the propeller thrust and Q_0 denotes the propeller power. Compared to the two-rotor configuration, operating the propellers of the four-rotor configuration produced lower thrust and required lower power input. The middle propellers carried slightly higher thrust due to the higher pitch angle. However, the overall vehicle power of the current four-rotor configuration, i.e. the propeller power values combined, was considerably higher than that of the two-rotor configuration.

It can also be noted that the overall thrust produced by the propellers of the four-rotor configuration was also considerably higher than that of the two-rotor configuration. This was mainly due to the additional drag of the aft propellers. Although stopped and feathered, the aft propellers produced a considerable amount of drag. Figure 16 shows the drag variations of the aft propeller at different feathering angles. The drag values were normalised using the propeller data

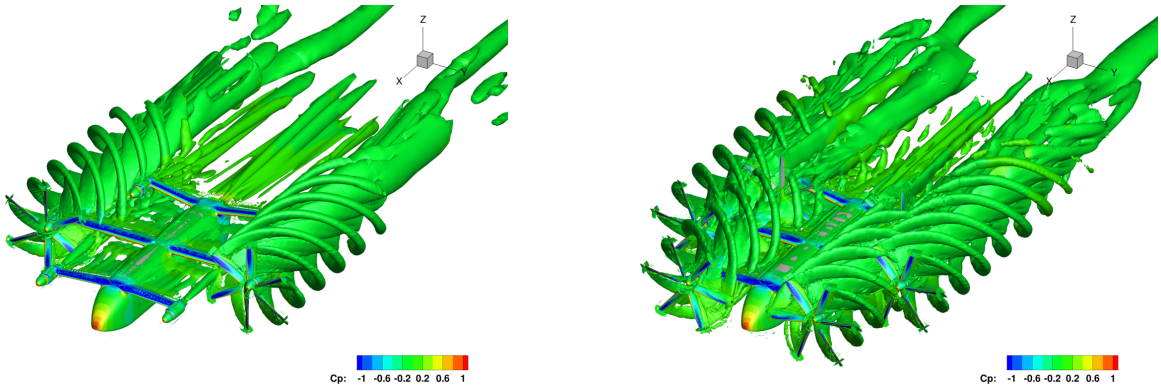

(a) Two-rotor configuration.

(b) Four-rotor configuration.

Figure 15: Instantaneous Q-criterion iso-surfaces of the two-rotor and four-rotor configurations in forward flight, coloured using pressure coefficient values.

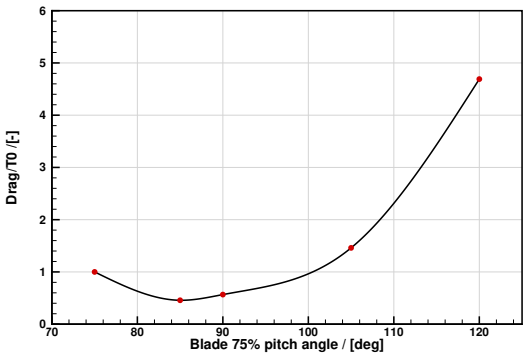

Figure 16: Aft propeller drag variations of the four-rotor configuration at different feathering angles.

of the two-rotor configuration. It can be observed that minimum drag of 0.5 T_0 can be acquired when the collective pitch angle of the blade is 85°. However, this minimum drag was still able to cancel out most of the thrust of the front propeller in the four-rotor configuration. Further decreasing or increasing the feather angle would both lead to significantly increased drag.

5.3 Near-field Acoustics

This section presents the near- and far-field acoustic features derived from the high-fidelity HMB3 solutions of the Skybus vehicle in forward flight, along with comparisons of the two- and four-rotor configurations. The near-field acoustics was directly extracted from the flow solution, while the far-field acoustics was computed using the HFWH2 code following the non-porous Farassat Formulation 1A, using the HMB3 surface pressure solutions as input.

First, the near-field acoustic analyses focused on the airframe surfaces to identify the noise sources. Figure 17(a) presents the instantaneous surface sound pressure values on the airframe of the two-rotor configuration in forward flight. Figure 17(b) presents the corresponding Root-Mean-Square (RMS) values of the surface acoustic signals and reflects the strength of the surface loading noise sources. The rotating blades were represented by wireframes to bring out features on the airframes. In figures 17(a) and 17(b), few loading noise sources on the airframe can be easily identified, i.e. outboard regions of the middle wing and the downstream nacelles. Correlating with the flow solutions in Figure 15(a), these regions coincided with the propeller wake impingement on the airframe and were mostly due to the aerodynamic interference. The fuselage and the upstream wing showed minor pressure fluctuations.

Figures 18(a) and 18(b) present the instantaneous

Table 5: Propeller and vehicle performance comparisons between the two-rotor and four-rotor configurations. All data was normalised using the propeller performance of the two-rotor configuration (T_0, P_0), where T_0 stands for the propeller thrust and P_0 denotes the propeller power.

Configuration	Propeller			Total Power
	Front	Middle	Aft	
Two-rotor	-	(T_0, P_0)	-	$2P_0$
Four-rotor	$(0.66T_0, 0.78P_0)$	$(0.88T_0, 0.92P_0)$	-	$3.4P_0$

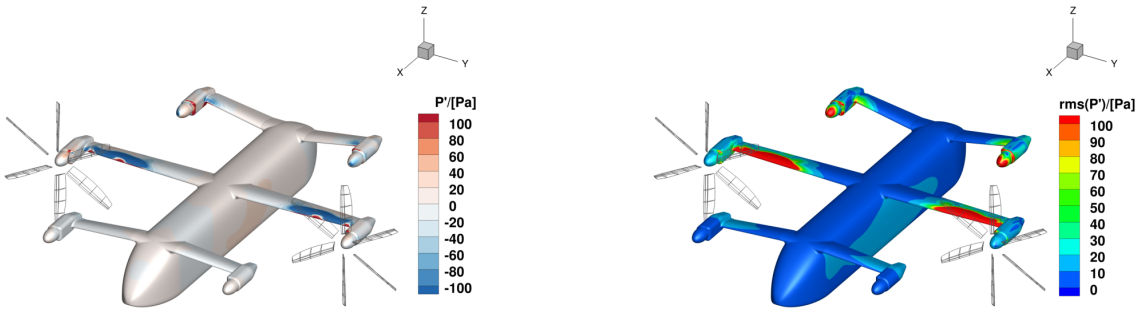

(a) Instantaneous surface sound pressure contours.

(b) Root-Mean-Square (RMS) values of the surface sound pressure contours.

Figure 17: Surface sound pressure contours and fluctuation levels on the airframe of the two-rotor configuration in forward flight. Moving blades are presented by wireframes.

sound pressure contours on the airframe of the four-rotor configuration in forward flight, and the corresponding RMS values. The operating front and middle propellers were also represented by wireframes to highlight results on the airframe. Compared to the two-rotor case, stronger surface pressure fluctuations were observed all over the airframe surface. The loading noise sources on the airframe were the front wings, the middle wings and nacelles, the aft wings and nacelles, and the stopped aft propeller blades. These regions also coincided with the propeller wakes of Figure 15(b), suggesting that these were also mainly results of aerodynamic interference.

Figures 19(a) and 19(b) present the acoustic Sound Pressure Levels (SPL) on a 15-metre-radius sphere enclosing the entire Skybus vehicle for the two-rotor and four-rotor configurations, respectively. The SPL values were computed directly from sound pressure signals extracted from the HMB3 simulations.

In Figure 19(a), for the two-rotor configuration, strong noise was perceived downstream the vehicle. This is consistent with the flow details of Figure 15(a). Another region of high noise was noted around the nose of the vehicle, on both starboard and port sides. This could be associated with the noise directivity of the propellers. The near-field acoustic patterns of this two-rotor configuration suggest that the vehicle is likely to produce strong noise when approaching and leaving.

In Figure 19(b), for the four-rotor configuration, it can be noticed that the levels were higher than that for the two-rotor case, and the acoustic directivity was considerably different. The acoustic levels of the four-rotor configuration were about 5 to 10 dB higher than the two-rotor case, in all directions. In terms of di-

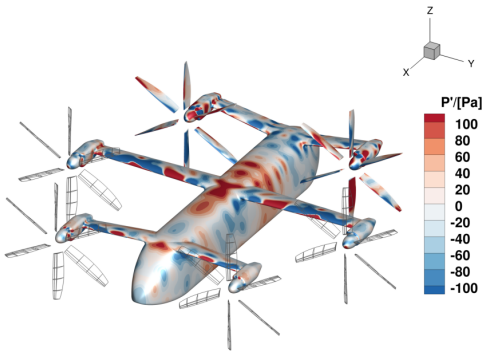

(a) Instantaneous surface sound pressure contours.

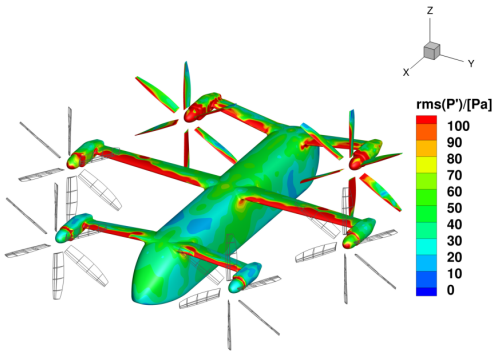

(b) Root-Mean-Square (RMS) values of the surface sound pressure contours.

Figure 18: Surface sound pressure contours and fluctuation levels on the airframe of the four-rotor configuration in forward flight. Moving blades are presented by wireframes.

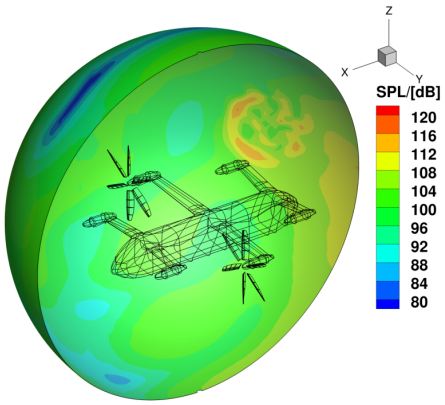

(a) Two-rotor configuration.

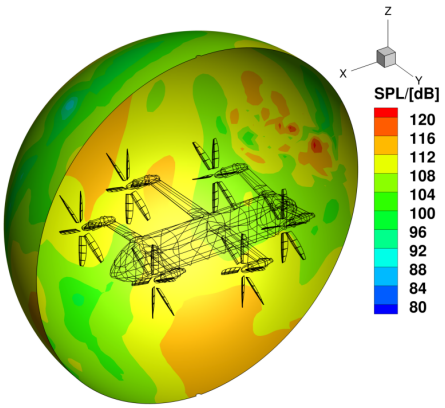

(b) Four-rotor configuration.

Figure 19: SPL contours on a 15-metre-radius sphere enclosing the vehicle.

rectivity, high noise levels were also perceived in the vehicle wake, which correlates well with the flow features in Figure 15(b). Strong noise was also perceived near the middle propellers in the lateral directions and below the vehicle.

5.4 Far-field Acoustics

Far-field acoustics of the two- and four-rotor configurations in forward flight were also computed. The acoustic propagation used the in-house HFWH2 code following the non-porous Farassat formulation 1A [26]. The far-field acoustic results contain the thickness and loading components. The unsteady, high-fidelity HMB3 flow solutions of the Skybus, along with the fully-resolved blade motions, were used as input panels into the HFWH2 code.

Figures 20(a) and 20(b) present the ground noise projection 1000 metres below the vehicle for the two-rotor and four-rotor configurations. The X axis represents the vehicle flight path, in level flight along the +X direction. The vehicle is set at the origin (0m, 0m) as denoted by the dash-dot lines. The +Y axis represents the port-side direction. The star-board side was not shown as the simulation was fully symmetric.

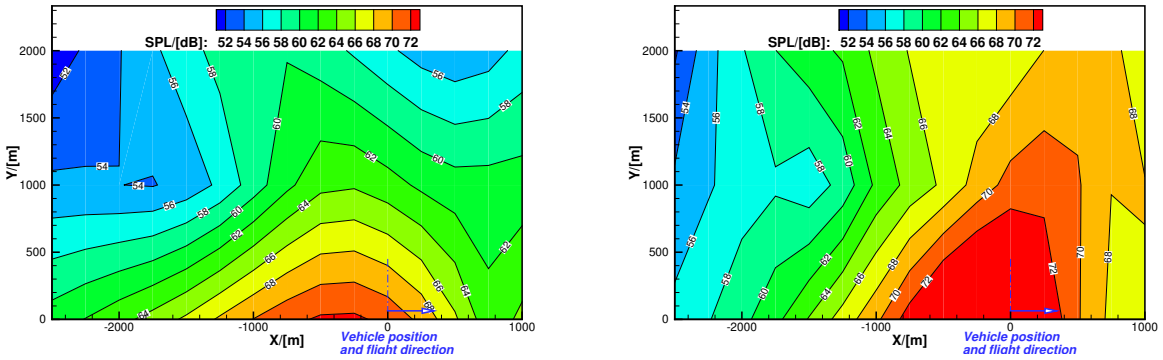

(a) Two-rotor configuration.

(b) Four-rotor configuration.

Figure 20: Far-field acoustic contours of the vehicle perceived 1000 metres below the vehicle.

In Figure 20(a), it can be noted the far-field acoustics of the two-rotor configuration, showed strong directivities towards the downstream and lateral directions. Along the vehicle longitudinal direction (X axis), the noise gradually increased when approaching. A maximum noise level of about 72 dB was perceived about 400 metres after the vehicle passage. The noise level gradually reduced to about 60 dB as the vehicle moved 2500 metres away. Along the lateral direction, the noise decayed quickly to about 60 dB beyond 1000 metres. A low noise region can be noted covering the area ($X < -1200m, Y > 700m$) with the noise level around 55 dB. These far-field noise features are consistent with the near-field solutions of Figure 19(a), as high near-field noise levels were observed near the vehicle nose and downstream.

Compared to the two-rotor configuration, the acoustic features of the four-rotor configuration, as shown in Figure 20(b), were considerably different. In the longitudinal direction, the vehicle noise gradually increased when approaching and led to a maximum level of 78 dB after the vehicle passage. The noise level decayed faster downstream compared to that of the two-rotor configuration. The noise level decayed to 56 dB, 2500 metres after the vehicle passage ($X < -2500m$). Along the lateral direction, for regions $-1000m < X < 1000m$, the noise decreased to about 68 dB beyond 1500 metres. The noise, however, decayed little along the lateral direction for regions with $X < -1000m$.

Figure 21 compares the acoustic features of the two- and four-rotor configurations along the flight path, i.e. the X axes in Figures 20(a) and 20(b). In Figure 21, both configurations showed similar acoustic features along the flight path, i.e. gradually increasing noise when approaching, maximum noise levels near the vehicle passage, and gradually reduced noise when moving away. The maximum noise levels were about 72 dB and 78 dB for the two- and four-rotor configurations, respectively. The four-rotor configuration showed consistently stronger noise than that of the two-rotor configuration when $X > -1000m$. It is interesting to notice that the noise level of the four-rotor configuration became lower for $X < -1000m$. This further reflected the differences in the noise directivities of the two configurations, as the four-rotor configuration projected more noise towards the lateral direction. These features are also consistent with the near-field acoustics of Figure 19(b).

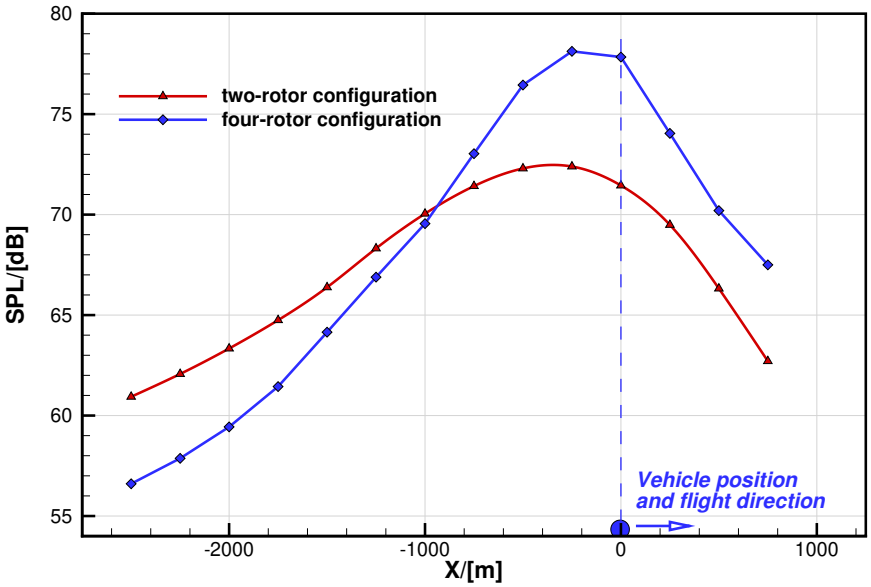

Figure 21: Acoustic levels of the two-rotor and four-rotor configurations along the flight path 1000 metres below.

6 Conclusions

This work presented the initial numerical, aerodynamic and acoustic, design and analysis of the heavy-lift Skybus eVTOL design. The vehicle propeller was first designed following a multi-fidelity approach. The complete Skybus vehicle in forward flight was then simulated, and two configurations were investigated. The following conclusions can be drawn from the present investigation:

1. A multi-fidelity approach was proposed and demonstrated for the propeller design of the Skybus vehicle. This method uses a combination of fast low-fidelity scans of the design space, and a high-fidelity gradient-based optimisation starting from the low-fidelity optima, thereby delivering final designs close to the global optima subject to constraints. Propeller designs with four, five, and six blades were first evaluated, and the six-bladed designs were found to be the most efficient. For the six-bladed propeller design of the Skybus vehicle, the low-fidelity stage brought a performance improvement of 3%, while the high-fidelity optimisation further boosted the performance by about 2.2% with negligible penalties in thrust.

2. The proposed propeller pitch-RPM maps were shown to be an efficient tool for performance visualisation and prediction for pitch- and RPM-regulated propellers. The performance maps are also used for efficient interpolations correlating various optimisations and performance scopes. In the present work, the performance maps helped deliver the propeller operating conditions of the Skybus in forward flight.

3. High-fidelity HMB3 simulations of the complete Skybus vehicle including the designed propellers in forward flight were also carried out. Two configurations with different numbers of operating propellers, i.e. the two- and four-rotor configurations, were investigated. For the studied operating conditions, the four-rotor configuration

showed considerably more complex aerodynamic interference mainly due to rotor-wing and rotor-rotor interactions. The total power required by the four-rotor configuration was about 1.7 times that of the two-rotor configuration.

4. In terms of acoustic features, both configurations projected noise of 70 to 75 dB to the ground in forward flight. The four-rotor configuration showed stronger noise due to aerodynamic interactions. The noise directivities of the two configurations were also different. The four-rotor configuration showed strong directivity towards the lateral directions, while the two-rotor configuration projected the noise mostly along the longitudinal direction. Due to these differences in directivity, along the flight path, the four-rotor configuration showed about 5 dB lower noise than the two-rotor configuration, 1000 metres after the vehicle passage.

Future design and analysis work on the Skybus concept will continue and more high-fidelity aerodynamic/acoustic analyses of the vehicle at various conditions will be delivered, aiming to refine the initial design.

Acknowledgement

The authors would like to acknowledge GKN Aerospace for their support and approval of publication.

Copyright Statement

Bibliography

[1] Higgins, R., Barakos, G., Shahpar, S., and Tristanto, I., "A computational fluid dynamic acoustic investigation of a tiltwing eVTOL concept aircraft," *Aerospace Science and Technology*, Vol. 111, 02 2021, pp. 106571.

[2] Arlen, L. and Gemmink, H., "CityAirbus, A Safe Entry into Remote Piloted Flight Test World," *47th European Rotorcraft Forum (virtual)*, 2021.

[3] Drela, M. and Youngren, H., "XROTOR user guide," http://web.mit.edu/drela/Public/web/xrotor/, 2003, available on-line.

[4] Youngren, H., Drela, M., and Sanders, S., "Ducted Fan Design Code," http://web.mit.edu/drela/Public/web/dfdc/, December 2005, Ducted Fan Design Code homepage, available on-line.

[5] Higgins, R. J., Zarev, A., Barakos, G. N., and Green, R. B., "Numerical investigation of a two-bladed propeller inflow at yaw," *Journal of Aircraft*, Vol. 57, No. 2, 2020, pp. 292–304.

[6] Biava, M. and Barakos, G. N., "Optimisation of ducted propellers for hybrid air vehicles using high-fidelity CFD," *The Aeronautical Journal*, Vol. 120, No. 1232, 2016, pp. 1632–1657.

[7] Zhang, T. and Barakos, G. N., "High-fidelity numerical analysis and optimisation of ducted propeller aerodynamics and acoustics," *Aerospace Science and Technology*, Vol. 113, 2021, pp. 106708.

[8] Zhang, T. and Barakos, G. N., "High-Fidelity CFD Validation and Assessment of Ducted Propellers for Aircraft Propulsion," *Journal of the American Helicopter Society*, Vol. 66, No. 1, 2021, pp. 1–28.

[9] Zhang, T. and Barakos, G. N., "Development of Simulation Tools for High Fidelity Analysis of Compound Rotorcraft," *AIAA Scitech 2020 Forum*, 2020, p. 1258.

[10] Steijl, R., Barakos, G. N., and Badcock, K., "A framework for CFD analysis of helicopter rotors in hover and forward flight," *International Journal for Numerical Methods in Fluids*, Vol. 51, No. 8, 2006, pp. 819–847.

[11] Biava, M., Woodgate, M., and Barakos, G. N., "Fully implicit discrete-adjoint methods for rotorcraft applications," *AIAA Journal*, Vol. 54, No. 2, 2015, pp. 735–749.

[12] Antoniadis, A., Drikakis, D., Zhong, B., Barakos, G., Steijl, R., Biava, M., Vigevano, L., Brocklehurst, A., Boelens, O., Dietz, M., et al., "Assessment of CFD methods against experimental flow measurements for helicopter flows," *Aerospace Science and Technology*, Vol. 19, No. 1, 2012, pp. 86–100.

[13] Steijl, R. and Barakos, G., "CFD analysis of complete helicopter configurations–lessons learnt from the GOAHEAD project," *Aerospace Science and Technology*, Vol. 19, No. 1, 2012, pp. 58–71.

[14] Han, D., Pastrikakis, V., and Barakos, G. N., "Helicopter flight performance improvement by dynamic blade twist," *Aerospace Science and Technology*, Vol. 58, 2016, pp. 445–452.

[15] Garcia, A. J. and Barakos, G. N., "Numerical simulations on the ERICA tiltrotor," *Aerospace Science and Technology*, Vol. 64, 2017, pp. 171–191.

[16] Jarkowski, M., Woodgate, M., Barakos, G., and Rokicki, J., "Towards consistent hybrid overset mesh methods for rotorcraft CFD," *International Journal for Numerical Methods in Fluids*, Vol. 74, No. 8, 2014, pp. 543–576.

[17] Menter, F., "Two-Equation Eddy-Viscosity Turbulence Models for Engineering Applications," *AIAA Journal*, Vol. 32, No. 8, 1993, pp. 1598–1605.

[18] Mavriplis, D. J., "Discrete adjoint-based approach for optimization problems on three-dimensional unstructured meshes," *AIAA journal*, Vol. 45, No. 4, 2007, pp. 741–750.

[19] Kraft, D., "Algorithm 733: TOMP-Fortran Modules for Optimal Control Calculations," *ACM Transactions on Mathematical Software*, Vol. 20, No. 3, 1994, pp. 262–281.

[20] Johnson, S., "The NLopt Nonlinear-Optimization Package," https://nlopt.readthedocs.io/en/latest/, retrieved 3 Sep 2020.

[21] Shepard, D., "A two-dimensional interpolation function for irregularly-spaced data," *Proceedings of the 1968 23rd ACM national conference*, 1968, pp. 517–524.

[22] Higgins, R. J., Jimenez-Garcia, A., Barakos, G. N., and Bown, N., "High-fidelity computational fluid dynamics methods for the simulation of propeller stall flutter," *AIAA Journal*, Vol. 57, No. 12, 2019, pp. 5281–5292.

[23] Zhang, T. and Barakos, G., "High-fidelity Numerical Investigation of Ducted Propeller Aerodynamics/Acoustics and Adjoint-based Design Optimisation," *77th Annual Forum of the Vertical Flight Society*, 2021.

[24] Chirico, G., Barakos, G. N., and Bown, N., "Propeller installation effects on turboprop aircraft acoustics," *Journal of Sound and Vibration*, Vol. 424, 2018, pp. 238 – 262.

[25] Ffowcs Williams, J. E. and Hawkings, D. L., "Sound generation by turbulence and surfaces in arbitrary motion," *Philosophical Transactions of the Royal Society of London. Series A, Mathematical and Physical Sciences*, Vol. 264, No. 1151, 1969, pp. 321–342.

[26] Farassat, F., "Derivation of Formulations 1 and 1A of Farassat," Tech. rep., NASA / TM-2007-214853, 2007.

[27] Dighe, V. V., Avallone, F., and van Bussel, G., "Effects of yawed inflow on the aerodynamic and aeroacoustic performance of ducted wind turbines," *Journal of Wind Engineering and Industrial Aerodynamics*, Vol. 201, 2020, pp. 104174.

[28] Smith, D. A., Filippone, A., and Barakos, G. N., "Acoustic Analysis of Counter-Rotating Open Rotors with a Locked Blade Row," *AIAA Journal*, 2020(avialable online).

[29] Zhang, T., Qiao, G., Smith, D., Barakos, G., and Kusyumov, A., "Parametric study of aerodynamic performance of equivalent ducted/un-ducted rotors," *Aerospace Science and Technology*, Vol. 117, 2021, pp. 106984.

[30] Drela, M. and Youngre, H., "Axisymmetric Analysis and Design of Ducted Rotors," http://web.mit.edu/drela/Public/web/dfdc/DFDCtheory12-31.pdf, December 2005, Ducted Fan Design Code theory, available on-line.

[31] Sacks, J., Schiller, S. B., and Welch, W. J., "Designs for Computer Experiments," *Technometrics*, Vol. 31, No. 1, 1989, pp. 41–47.

[32] Bouhlel, M. A., Hwang, J. T., Bartoli, N., Lafage, R., Morlier, J., and Martins, J. R. R. A., "A Python surrogate modeling framework with derivatives," *Advances in Engineering Software*, 2019, pp. 102662.